Effective properties of periodic plate-array metacylinders

H. J. Putley ◉,[*] S. Guenneau ◉, R. V. Craster, and B. Davies

Department of Mathematics, Imperial College London, 180 Queen's Gate, South Kensington, London SW7 2AZ, United Kingdom

C. G. Poulton

School of Mathematical and Physical Sciences, University of Technology Sydney, 15 Broadway, Ultimo, New South Wales 2007, Australia

We use semianalytic methods to model a periodic structure of plate-array cylinders (metacylinders), and derive several of the medium's effective material properties in the quasistatic limit. Subject to *s*-polarized [transverse-electric (TE)] light, the anisotropic dispersion of the crystal manifests as a Maxwell Garnett equation for the effective permittivity at leading order. This is performed both for the case of no material contrast between interior and exterior regions, and a nonunity normalized refractive index. In each case, the leading order effective permittivity is a function of the difference between Bloch wave and plate-array angles. As such, we envisage the metamaterial as being mechanically tunable through uniform mechanical rotation of the constituent metacylinders.

I. INTRODUCTION

Composite materials can be treated as effectively continuous and homogeneous when the characteristic cell, and hence the crystalline elements therein, are of a subwavelength scale. The long-range uniformity of the crystalline elements gives rise to effective properties at the macroscale, a process not dissimilar to magnetism induced by the long-range ordering of magnetic dipoles. One such example is the classical photonic crystal of dielectric cylinders, for which the leading order estimate of the effective permittivity is given by the Lorentz-Lorenz formula [1,2]. The same analysis can be applied to metamaterials, for which the uniformity of the constituent "meta-atoms" gives rise to exotic effective properties. These include negative effective permeability μ_{eff} and a magnetic response [3], negative effective permittivity ε_{eff} [4], and hence left-handed materials [5–7]. These in turn have been proposed to facilitate a myriad of devices, including flat lenses [8], invisibility cloaks [9,10], and a superlens utilizing all-angle negative refraction [11].

Of recent interest have been metamaterials that allow for a tunable response [13–15], particularly active metasurfaces that hold pixel-level programmability [16]. One such example is two-dimensional (2D) crystals of meta-atoms of a multilayered cylindrical geometry [17,18]. The hyperbolic metamaterial of [17] can be tuned to significantly enhance the scattering cross section compared to a cylinder of

homogeneous composition. Very recently, the authors of [18] considered a crystal of metamaterial cylinders consisting of both graphene and multilayered metasurfaces, and were able to demonstrate a number of exotic features, including a tunable hyperbolic dispersion relation and a double negative response. In [17,18] the tunability is demonstrated by changing the material parameters to modify the macroscopic response. The review articles [19,20] discuss alternative methods for achieving tunability, including geometrical or structural tuning of the crystalline elements or unit cell. The macroscopic response of a composite metasurface depends on the size and orientation of its constituent elements, providing scope to alter the effective material parameters actively via mechanical adjustment. As pointed out in [20], such mechanical adjustments can be challenging because a physical mechanism is necessary to manipulate the crystalline elements. A number of methods have been proposed for mechanical reconfiguration, including mechanical deformation of an elastic substrate or matrix [21–24] and use of pneumatic actuators [25]. Alternative methods include thermomechanical [26], electromechanical, [27] and photoresponsive [28] control, among others.

In this article, we present an analysis of a periodic medium that is composed of plate-array cylinders; see Fig. 1 for typical eigenmodes of the crystal and Fig. 2(a) for a 3D schematic. The plate-array cylinders consist of a dielectric sandwiched between a set of metallic, closely spaced thin plates. The analysis is performed in the quasistatic limit of vanishing wave number, such that the wavelength is much larger than the characteristic cell dimension. In this limit the plate-array cylinders, or "metacylinders", are described by an effective medium model. The acoustic mode is used to determine the homogenized properties of the crystal, and for this mode it is assumed that there exists a linear relationship $k \propto k_0$ as $k_0 \to 0$, where k is the wave number in the bulk exterior
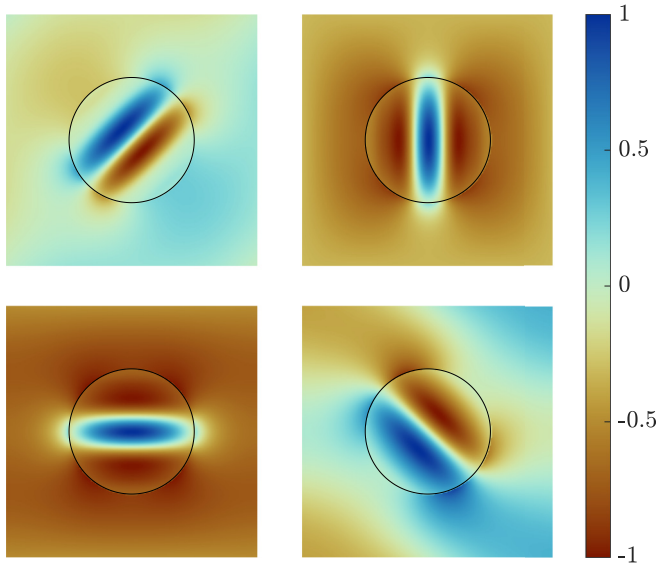
---

[*]h.putley18@imperial.ac.uk

FIG. 1. Longitudinal magnetic fields H_z of the plate-array crystal in the zeroth cell for different plate-array orientations, corresponding to the Eigenmodes of (22). Color maps here and throughout are from [12].

and k_0 is the Bloch wave number of the eigenmodes. The plate-array medium induces anisotropic dispersion of light through the crystal which, due to the long-range uniformity of the crystalline elements, manifests as an acoustic branch that is elliptical. The eccentricity of these elliptical solutions is a function of the effective permittivities along the principal crystalline axes, a result of the metacylinder favoring scattering in a direction perpendicular to the plate array [29,30]. Here it is shown that the effective electrical permittivity is a function of the crystalline filling fraction, the material contrast and, crucially, the difference in angle between the Bloch mode and the uniform plate-array medium. It is due to this angular dependence that we label this crystal a mechanically programmable metasurface.

This paper is organized as follows: Section II defines the structure of the periodic medium and the zeroth cell. Section III provides the formulas for the interior and exterior fields, before matching these at the cylindrical surface to yield a linear system of equations for the unknown coefficients. The crystal is homogenized in Sec. IV, in which the infinite system is truncated to form an 8×8 "dipole" matrix. Section V details the expansion of the dipole matrix determinant, from which a pair of Maxwell Garnett equations for the permittivity are recovered at leading order for the cases of no material contrast and nonunity material contrast. This is followed by comparison with numerics conducted using both a multipole implementation and FEM computations. We state our conclusions in Sec. VI. Appendixes A and B detail the plate-array homogenization and the small wave number expansions of the dipole matrix elements, respectively.

II. CRYSTALLINE STRUCTURE

The periodic medium, depicted in Fig. 2(a), consists of metacylinders of a plate-array microstructure, and is of
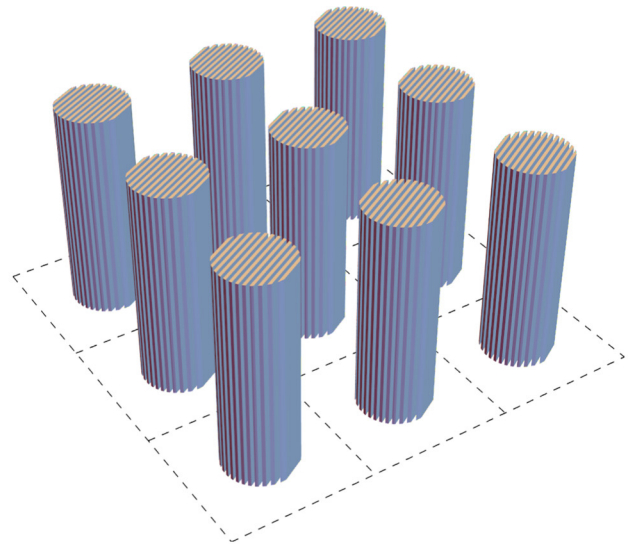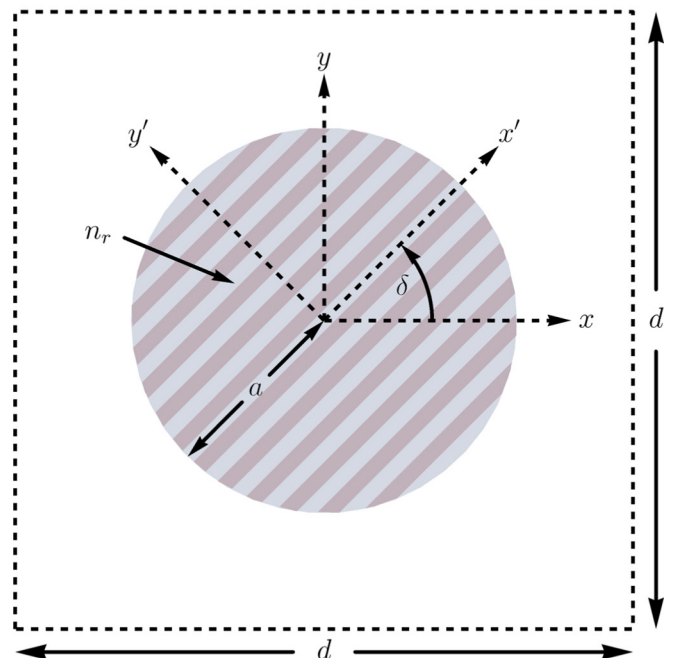
FIG. 2. (a) A portion of the crystal consisting of plate-array metacylinders arranged in a square lattice. (b) Metacylinder geometry: plates are depicted in dark gray and interstitial dielectric in light blue. Plate number and thickness are for illustrative purposes only.

infinite extent in the (x, y) plane. The metacylinders are of a circular cross section of uniform radius a, have uniform plate-array orientation δ, and extend infinitely in z without twist or bend. The crystal is subject to s-polarized [or equivalently transverse-electric (TE) polarized] light under normal incidence, i.e., (E_x, E_y, H_z). We assume time-harmonic solutions of the form

$$\mathbf{V}(\mathbf{r}, t) = \mathbf{V}(\mathbf{r})e^{-i\omega t} \qquad (1)$$

where $\mathbf{V}$ can be either $\mathbf{H}$ or $\mathbf{E}$ and $\mathbf{r}$ is the position vector in two-dimensional cylindrical coordinates $\mathbf{r} = (r, \theta)$. Using the ansatz (1), we need only solve for the magnetic or electric field in the plane, and do so by eliminating for $\mathbf{H}$ in Maxwell's equations to yield the following pair of Helmholtz equations [31]:

$$\left(\nabla^2 + n_r^2 k^2\right) H_z^{\text{int}} = 0 \quad \text{in } r < a, \tag{2}$$

$$\left(\nabla^2 + k^2\right) H_z^{\text{ext}} = 0 \quad \text{in } r > a, \tag{3}$$

where the interior and exterior regions have been regarded separately with superscripts "int" and "ext", $k = |\mathbf{k}|$, and ∇^2 is the Laplacian in two-dimensions. In Eq. (2), which applies before homogenization of the plate array, the quantity n_r refers to the refractive index of the interior interstitial medium between the plates normalized with respect to that of the exterior bulk. We add that, in homogenizing the periodic medium in the quasistatic limit, we will eventually assume that the crystalline structure is dilute; this corresponds to the area fraction $f \ll 1$ of the cylinders. In fact, we find that it is possible with our method to consider area fractions $f \leqslant 0.5$.

A schematic of the metacylinder is provided in Fig. 2(b), which details the plate-array geometry and unit cell structure. The plates are oriented at an angle δ with respect to the x axis, which defines the directions of the primed coordinates (x', y'): x' is parallel and y' is perpendicular to the plate array. The plates in Figs. 2(a) and 2(b) are only illustrative; the metacylinder is homogenized under the assumptions that there are a large number of plates occupying the circular cross section, that the plates are very thin, and that the spacing between the plates d_p is small. The metacylinder is therefore treated as an *effective medium*, with a modified wave equation in the interior and a pair of continuity conditions at the surface. This homogenization is carried out in Sec. III B and Appendix A.

III. FIELD EQUATIONS

A. The exterior domain

Solutions satisfying (3) can be written as a sum over the direct lattice of multipole expansions in cylindrical harmonics:

$$H_z^{\text{ext}} = \sum_j \sum_{m \in \mathbb{Z}} b_{j,m} \hat{\psi}_{j,m}(k, \mathbf{r}_j), \tag{4}$$

which holds in the region exterior to the set of cylinders. Here $b_{j,m}$ are the multipole moments of cylinder j, the function $\hat{\psi}_{j,m} = H_m(kr_j)e^{im\theta_j}$ represents an outgoing wave, and $H_m(x) \equiv H_m^{(1)}(x)$ is the Hankel function of the first kind, such that (4) satisfies the Sommerfeld radiation condition [32]:

$$\lim_{r \to \infty} r^{\frac{1}{2}} \left(\frac{\partial}{\partial r} - ik \right) H_z^{\text{ext}}(r, \theta) = 0. \tag{5}$$

The outer sum in (4) is over all cylinders j and the inner sum is over multipole moments, with $m = 0$ being the monopole moment, $m = \pm 1$ the dipole moments, etc. Eq. (4) is known as the Wijngaard formula [33], which asserts that in the absence of any external sources the total field exterior to a set of cylinders may be written as the sum over the scattered fields in their respective cylinder coordinates $\mathbf{r}_j = (r_j, \theta_j)$.

The periodicity of the lattice implies that waves in propagation through the crystal will be of Bloch-periodic form:

$$b_{j,m} = b_{0,m} e^{i\mathbf{k}_0 \cdot \mathbf{R}_j}, \tag{6}$$

where the direct lattice vectors $\mathbf{R}_j = (R_j, \phi_j)$. Separating the $j = 0$ and $j \neq 0$ terms in (4) and applying Graf's addition theorem [34] [p. 363, Eq. (9.1.79)], allows for the total field in the exterior domain to be written in the well-known form [1]

$$H_z^{\text{ext}}(k, \mathbf{r}) = \sum_{m \in \mathbb{Z}} b_m H_m(kr)e^{im\theta}$$
$$+ \sum_{m \in \mathbb{Z}} b_m \sum_{q \in \mathbb{Z}} S_{m-q}(-1)^{m-q} J_q(kr)e^{iq\theta}, \tag{7}$$

where $b_m \equiv b_{0,m}$ refers to the zeroth cell of coordinates (r, θ) and

$$S_l(k, \mathbf{k}_0) = \sum_{j \neq 0} H_l(kR_j)e^{il\phi_j}e^{i\mathbf{k}_0 \cdot \mathbf{R}_j} \tag{8}$$

is the lattice sum in direct space. Equation (7) can be simplified by writing $S_l = S_l^J + iS_l^Y$, where

$$S_l^J(k, \mathbf{k}_0) = \sum_{j \neq 0} J_l(kR_j)e^{il\phi_j}e^{i\mathbf{k}_0 \cdot \mathbf{R}_j}, \tag{9}$$

$$S_l^Y(k, \mathbf{k}_0) = \sum_{j \neq 0} Y_l(kR_j)e^{il\phi_j}e^{i\mathbf{k}_0 \cdot \mathbf{R}_j}. \tag{10}$$

It can be shown that

$$S_l^J(k, \mathbf{k}_0) = -\delta_{l,0}. \tag{11}$$

Substitution of (9)-(11) into (7) yields the following expression for the total field in the exterior domain:

$$H_z^{\text{ext}}(k, \mathbf{r}) = \sum_{m \in \mathbb{Z}} ib_m Y_m(kr)e^{im\theta}$$
$$+ \sum_{m \in \mathbb{Z}} ib_m \sum_{q \in \mathbb{Z}} S_{m-q}^Y(-1)^{m-q} J_q(kr)e^{iq\theta}. \tag{12}$$

The sum S_l^Y is conditionally convergent at all orders l, but in previous work by Chin *et al.* [35] has been recast as an absolutely convergent sum in reciprocal space:

$$S_l^Y(k, \mathbf{k}_0) J_l(k\xi) = -Y_0(k\xi)\delta_{l,0}$$
$$- \frac{4}{A} i^l \sum_h \frac{J_l(Q_h\xi)}{Q_h^2 - k^2} e^{il\theta_h}, \tag{13}$$

where $\boldsymbol{\xi}$ is an arbitrary vector in the unit cell such that $|\boldsymbol{\xi}| < |\mathbf{R}_j|$ for all $j \neq 0$, $\mathbf{Q}_h = (Q_h, \theta_h) = \mathbf{K}_h + \mathbf{k}_0$, where $\mathbf{K}_h$ are the reciprocal lattice vectors, and A is the unit-cell area. The derivation of (13) is not provided here but is given in detail in [1,35,36], and comes from a consideration of the spatial and spectral domains' Green's functions. The convergence of (13) has been accelerated by successive integrations as in [37]. The following relation of S_l^Y can be seen from (8) and is particularly useful:

$$S_{-l}^Y = S_l^{Y*}, \tag{14}$$

where $*$ denotes the complex conjugate.

B. The interior domain

The plate array within the cylinders is replaced by an effective medium description encapsulated by three equations: a one-dimensional wave equation in the interior and a pair of continuity conditions at the surface. Assuming that the interplate spacing d_p is much smaller than both the length of the plates and the wavelength (i.e., $n_r k d_p \ll 1$), the Helmholtz equation in the interior domain (2) can be expanded in powers of the small parameter $\zeta = n_r k d_p$ to yield the following wave equation at second-order:

$$\left(\frac{\partial^2}{\partial x'^2} + n_r^2 k^2 \right) H_z^{\text{int}}(x', y') = 0, \tag{15}$$

where n_r is the refractive index of the interstitial medium between the plates normalized with respect to the background medium, and (x', y') are the plate-array coordinates. A caveat of this homogenization is that a Neumann boundary condition on the plates' surfaces is necessary to ensure the omission of the second-order derivative in the y' coordinate in (15), hence the choice of metallic plates and of TE polarization. The derivation of (15) is provided in Appendix A and alternatively in [29,38].

Solutions of (15) comprise the superposition of forwards and backwards traveling waves:

$$H_z^{\text{int}}(x', y') = C(y')e^{i n_r k x'} + D(y')e^{-i n_r k x'} \tag{16}$$

where $C(y')$, $D(y')$ are the waves' amplitudes. In order to apply the matching conditions on the cylindrical boundary $r = a$ it is necessary to replace the primed plate-array coordinates with polar coordinates:

$$H_z^{\text{int}}(a, \theta) = C(\theta)e^{i n_r k a \cos(\theta - \delta)} + D(\theta_0)e^{-i n_r k a \cos(\theta - \delta)}, \tag{17}$$

where we have used $x' = r \cos(\theta - \delta)$ and replaced the amplitudes $C(y')$, $D(y')$ with equivalent quantities $C(\theta)$, $D(\theta)$ that have an explicit dependence on the angular coordinate. By symmetry about the y' axis,

$$C(\theta) = C(\pi + 2\delta - \theta), \tag{18a}$$

$$D(\theta) = D(\pi + 2\delta - \theta), \tag{18b}$$

which is an expression of the fact that the surfaces of the semicircles $\theta \in [\delta - \pi/2, \delta + \pi/2]$ and $\theta \in [\delta + \pi/2, \delta + 3\pi/2]$ are connected by the interior plate array. Writing $y' = a \cos(\theta - \delta - \pi/2)$, we approximate these amplitudes by expansions in Chebyshev polynomials:

$$\{C(\theta), D(\theta)\} = \sum_{n=0}^{\infty} \{c_n, d_n\} T_n \left(\frac{y'}{a} \right)$$

$$= \sum_{n=0}^{\infty} \{c_n, d_n\} \cos \left[n \left(\theta - \delta - \frac{\pi}{2} \right) \right], \tag{19}$$

which satisfies (18). Here the $\{x, y\}$ notation is shorthand for the respective equations for quantities x and y. Substitution of (19) into (17) and utilizing the Jacobi-Anger expansion [39] [Eq. (3.89)] allows for the field on the interior boundary to be expressed as

$$H_z^{\text{int}}(a, \theta)$$
$$= \sum_{n=0}^{\infty} c_n \cos \left(n \left(\theta - \delta - \frac{\pi}{2} \right) \right) \sum_{m \in \mathbb{Z}} i^m J_m(n_r k a) e^{im(\theta - \delta)}$$
$$+ \sum_{n=0}^{\infty} d_n \cos \left(n \left(\theta - \delta - \frac{\pi}{2} \right) \right) \sum_{m \in \mathbb{Z}} (-i)^m J_m(n_r k a) e^{im(\theta - \delta)} \tag{20}$$

for which we note the necessity of the interior field being expressed in multipole expansions of regular waves so as to avoid the occurrence of a singularity as $a \to 0$.

Assuming that both the wave number k and the interstitial spacing d_p are small, the homogenized wave equation (15) will break down under two scenarios. The first is that in which the relative index $n_r \gg 1$, in which case the small parameter $\zeta \gtrsim \mathcal{O}(1)$ and the homogenization carried out in Appendix A is no longer valid. What is more, the plate-array cylinders undergo resonance at and above $n_r k a = \pi/2$ (the wave number at which an integer number of half wavelengths navigate the centralmost channel), and as n_r is increased the resonant wave number is pushed towards $k = 0$. This invalidates the assumed linear relationship between k and k_0 as $k_0 \to 0$. The second scenario in which (15) fails is when $n_r \ll 1$, in which case there is an additional small parameter in the equation (A3), $n_r k$. Assuming $n_r k \simeq \zeta$ and using ansatz (A5), one will instead recover Laplace's equation at leading order rather than an equation of the form (15). To avoid both scenarios we keep $n_r = \mathcal{O}(1)$ in our computations.

C. Continuity conditions

The effective medium description is closed by a pair of continuity conditions across the cylindrical surface. These are of the form

$$H_z^{\text{ext}} = H_z^{\text{int}} \quad \text{on } r = a, \tag{21a}$$

$$\frac{\partial H_z^{\text{ext}}}{\partial r} = \cos(\theta - \delta) \frac{1}{n_r^2} \frac{\partial H_z^{\text{int}}}{\partial x'} \quad \text{on } r = a, \tag{21b}$$

where (21a) is the field continuity and (21b) the flux continuity of the magnetic field through the cylinder. The latter flux condition arises from a consideration of the interior flux component along the radial direction, whereas the former arises from continuity of the tangential field components through the curved surface; see [40] [Eqs. (2.7)–(2.16)] or [41]. Substitution of (12) and (20) into (21a) and (21b) and making use of the orthogonality of the cylindrical harmonics allows us to form an infinite system of equations for the unknowns b_m, c_n, and d_n:

$$i b_p \frac{Y_p(ka)}{J_p(ka)} + \sum_{m \in \mathbb{Z}} i b_m S_{m-p}^Y (-1)^{m-p} - \frac{1}{2} e^{ip(\frac{\pi}{2} - \delta)} \sum_{n=0}^{\infty} [c_n(-1)^n + d_n(-1)^p] \frac{J_{p-n}(n_r k a) + J_{p+n}(n_r k a)}{J_p(ka)} = 0, \tag{22a}$$

$$ib_p \frac{Y'_p(ka)}{J'_p(ka)} + \sum_{m\in\mathbb{Z}} ib_m S^Y_{m-p}(-1)^{m-p} - \frac{1}{2} e^{ip(\frac{\pi}{2}-\delta)} \sum_{n=0}^{\infty} [c_n(-1)^n + d_n(-1)^p] \frac{J'_{p-n}(n_r ka) + J'_{p+n}(n_r ka)}{n_r J'_p(ka)} = 0. \qquad (22\text{b})$$

Here, the prime refers to the derivative with respect to the radial coordinate. The first two terms in both (22a) and (22b) resemble the Rayleigh system under Dirichlet and Neumann boundary conditions, respectively [1,41]. The system formed by (22) is truncated as $(m,p) \in [-M-1,\dots,M]$ and $n \in [0,\dots,M]$, where M is the truncation point of the multipole and Chebyshev expansions, so as to arrive to a system of equations of dimension $(4M+4)$. Setting the determinant of the truncated system to zero recovers the dispersion relation between k and k_0.

IV. DIPOLE APPROXIMATION

A. The dipole system

Under the assumption that the crystal is dilute it is reasonable to approximate the solutions (12) and (20) by the first few terms in their respective expansions. Truncating (22) at $M=1$ we are left with only the $(m,p) \in [-2,-1,0,1]$ and $n \in [0,1]$ terms (we retain one quadrupole moment to ensure that the matrix is square), which form the following 8×8 system of equations:

$$\mathbf{T} := \left(\begin{array}{cccc|cccc}
M_2 + S^Y_0 & -S^Y_1 & S^Y_2 & -S^Y_3 & C_{-2,0} & C_{-2,1} & D_{-2,0} & D_{-2,1} \\
-S^{Y*}_1 & M_1 + S^Y_0 & -S^Y_1 & S^Y_2 & C_{-1,0} & C_{-1,1} & D_{-1,0} & D_{-1,1} \\
S^{Y*}_2 & -S^{Y*}_1 & M_0 + S^Y_0 & -S^Y_1 & C_{0,0} & C_{0,1} & D_{0,0} & D_{0,1} \\
-S^{Y*}_3 & S^{Y*}_2 & -S^{Y*}_1 & M_1 + S^Y_0 & C_{1,0} & C_{1,1} & D_{1,0} & D_{1,1} \\
\hline
M'_2 + S^Y_0 & -S^Y_1 & S^Y_2 & -S^Y_3 & C'_{-2,0} & C'_{-2,1} & D'_{-2,0} & D'_{-2,1} \\
-S^{Y*}_1 & M'_1 + S^Y_0 & -S^Y_1 & S^Y_2 & C'_{-1,0} & C'_{-1,1} & D'_{-1,0} & D'_{-1,1} \\
S^{Y*}_2 & -S^{Y*}_1 & M'_0 + S^Y_0 & -S^Y_1 & C'_{0,0} & C'_{0,1} & D'_{0,0} & D'_{0,1} \\
-S^{Y*}_3 & S^{Y*}_2 & -S^{Y*}_1 & M'_1 + S^Y_0 & C'_{1,0} & C'_{1,1} & D'_{1,0} & D'_{1,1}
\end{array} \right)
\left(\begin{array}{c}
b_{-2} \\ b_{-1} \\ b_0 \\ b_1 \\ c_0 \\ c_1 \\ d_0 \\ d_1
\end{array} \right) = \mathbf{0}. \qquad (23)$$

Here, the following quantities have been defined:

$$M_p = \frac{Y_p(ka)}{J_p(ka)}, \quad M'_p = \frac{Y'_p(ka)}{J'_p(ka)}, \qquad (24\text{a})$$

$$\{C_{p,n}, D_{p,n}\} = \mathcal{I}_{p,n} \frac{J_{p-n}(n_r ka) + J_{p+n}(n_r ka)}{2 J_p(ka)}, \qquad (24\text{b})$$

$$\{C'_{p,n}, D'_{p,n}\} = \mathcal{I}_{p,n} \frac{J'_{p-n}(n_r ka) + J'_{p+n}(n_r ka)}{2 n_r J'_p(ka)}, \qquad (24\text{c})$$

where $\mathcal{I}_{p,n} = (-1)^{\{n,p\}} i^{p+1} e^{-ip\delta}$. M_p and M'_p are referred to as the *boundary* coefficients and $C_{p,n}$, $C'_{p,n}$, $D_{p,n}$ and $D'_{p,n}$ are the *interior* coefficients. Examining (24a) it is clear from the Bessel function relations [42] that $M_{-p} = M_p$ and $M'_{-p} = M'_p$. Lattice sums of a negative order have been replaced by the complex conjugate of lattice sums of positive order by (14).

B. Homogenization

In homogenizing an isotropic medium the standard approach [1,40,43–46] is to examine the behavior of the lowest wave number band in the limit $k_0 \to 0$, for which it is assumed that there exists a proportionality between the bulk exterior wave number and Bloch wave number of the form

$$k = \alpha k_0, \qquad (25)$$

where $k_0 = |\mathbf{k}_0|$ and α is a scalar coefficient. The physical interpretation of α comes from a consideration of the phase difference across the unit cell [43], with a corresponding phase

refractive index:

$$n_{\text{eff}} = \frac{1}{\alpha} \qquad (26)$$

for which the label *effective* asserts that the periodic medium can be described as effectively continuous with macroscopic material parameter n_{eff}. Thus,

$$k = \frac{1}{n_{\text{eff}}} k_0. \qquad (27)$$

The form of α, and hence n_{eff}, is deduced by utilizing the following expansion [2]:

$$\alpha = \alpha_0 + \alpha_2 (k_0 d)^2 + \mathcal{O}(k_0 d)^4, \qquad (28)$$

where classically the leading order term α_0 encapsulates the dependence on the area fraction f of the cylinders, or the dielectric contrast across the cylindrical surface [1]. α_2 specifies the wave number dependence of α and provides the first dynamic correction term to the medium's effective permittivity. At finite frequency this dependence is assumed to be quadratic, hence $\alpha_1 = 0$. Herein we seek to determine only the leading order term α_0 and hence only the leading order effective permittivity in the form of a Maxwell Garnett equation.

For an anisotropic medium on the other hand, the meaning of α is connected with the definition of the effective dielectric tensor, which when diagonalized along the principal axes is of

the form

$$\boldsymbol{\varepsilon}_{\text{eff}} = \begin{pmatrix} \varepsilon_1 & 0 \\ 0 & \varepsilon_2 \end{pmatrix}, \tag{29}$$

where ε_1 and ε_2 are the principal permittivities of the crystal. Assuming that the material is magnetically isotropic, (29) can be recast in terms of an effective refractive index tensor:

$$\mathbf{n}_{\text{eff}} = \begin{pmatrix} n_1 & 0 \\ 0 & n_2 \end{pmatrix}, \tag{30}$$

where n_1 and n_2 are the principal refractive indices of the crystal such that $n_1 = \sqrt{\varepsilon_1}$, $n_2 = \sqrt{\varepsilon_2}$. The relationship (27) in vector form is

$$\mathbf{k} = \mathbf{n}_{\text{eff}}^{-1} \mathbf{k}_0 = \begin{pmatrix} \frac{1}{\sqrt{\varepsilon_1}} & 0 \\ 0 & \frac{1}{\sqrt{\varepsilon_2}} \end{pmatrix} \mathbf{k}_0. \tag{31}$$

To obtain an equation of the form (25) we take the magnitude of the left- and right-hand sides:

$$|\mathbf{k}| = \left(\frac{1}{\varepsilon_1} \cos^2(\theta_0 - \delta) + \frac{1}{\varepsilon_2} \sin^2(\theta_0 - \delta) \right)^{\frac{1}{2}} |\mathbf{k}_0|$$
$$= \alpha |\mathbf{k}_0|, \tag{32}$$

where we have written the Bloch vector $\mathbf{k}_0$ as

$$\mathbf{k}_0 = \begin{pmatrix} k_0 \cos(\theta_0 - \delta) \\ k_0 \sin(\theta_0 - \delta) \end{pmatrix}. \tag{33}$$

The definition (33) aligns the principal axes of the crystal with the rotated plate-array coordinates. Denoting the principal axes' directions as $1 \equiv x'$ and $2 \equiv y'$, then the principal permittivities can be recovered from (32) by choosing $\theta_0 = \delta$ for $\varepsilon_{x'}$ and $\theta_0 = \delta + \pi/2$ for $\varepsilon_{y'}$. The remaining challenge is to deduce the form of α by substitution of (32) into the dipole system (23), and examining the behavior of $|\mathbf{T}| = 0$ in the limit $k_0 \to 0$, where $\mathbf{T}$ is the 8×8 matrix given in (23).

In determining the small k_0 expansion in α the coefficients (24) and lattice sums (13) require series expansions in small k and k_0. The boundary coefficients (24a) occur for orders $p \in [0, 1, 2]$, for which the small k expansions are available in Appendix B 1. The interior coefficients (24b) and (24c) occur for orders $p \in [-2, \dots, 1]$, $n \in [0, 1]$, and like the boundary coefficients require small k expansions for ratios of Bessel functions. These can be found in Appendix B 2.

The method by which the lattice sums are approximated requires a series expansion of (13) to order k^0 for orders $l \in [0, \dots, 3]$. This involves separation of the $h = 0$ and $h \neq 0$ terms before using Graf's addition theorem [34] on the latter sum to yield an expansion in terms of k_0. Subsequently, the method makes use of a set of recurrence relations for the lattice sums inherent in the expression to arrive to leading order approximations. This is carried out in Appendix B 3, and follows the method set out in [40].

V. RESULTS

We seek the leading order terms for small k, k_0 in the expansion of $|\mathbf{T}| = 0$. This is achieved by implementing the approximations (B1)–(B4), (B10), (32), and (28) into (23). Computing the determinant of this 8×8 matrix by hand is intractable, so we make use of *Wolfram Mathematica* [47] to carry out the expansion of $|\mathbf{T}|$ analytically. This script is available in the Supplemental Material [48]. By replacing a with the area fraction of the metacylinders f, according to $a = \sqrt{fd^2/\pi}$, then solving for α_0 we arrive at a Maxwell Garnett equation that describes the leading order behavior of the crystal. We distinguish between the cases $n_r = 1$ and $n_r \neq 1$ in the following two subsections, since the resulting effective material parameters take a much more elegant form in the first case.

A. The case $n_r = 1$

In the case of $n_r = 1$ the leading order term in the expansion of $|\mathbf{T}|$ is of the form

$$T_{-12} = \frac{2^{15} 3 e^{2i\delta} \pi^2 \{(1+f)\alpha_0^2 - 1 - f \cos[2(\delta - \theta_0)]\}}{f^6 k_0^{12} d^{12} \alpha_0^{12} (\alpha_0^2 - 1)}, \tag{34}$$

where T_ν denotes the $\mathcal{O}(k_0^\nu)$ term. Solving (34) for α_0 by equating the left-hand side to zero, we have

$$\alpha_0 = \sqrt{\frac{1 + f \cos[2(\delta - \theta_0)]}{1 + f}}. \tag{35}$$

The form of (35) makes clear that the anisotropy of the crystal is a leading order effect and is due to the interplay of the difference in incident and plate-array angles and the area fraction of the cylinders. We can also define an associated *scalar* effective permittivity:

$$\varepsilon_{\text{eff}}^0 = \frac{1 + f}{1 + f \cos[2(\delta - \theta_0)]}. \tag{36}$$

Equation (36) has the form of a Maxwell Garnett equation, and is related to the elements of the effective permittivity tensor by way of (32)

$$\varepsilon_{x'} = 1, \tag{37a}$$

$$\varepsilon_{y'} = \frac{1 + f}{1 - f}. \tag{37b}$$

Accordingly, light propagating through the crystal will find it to be transparent along the x' direction and will undergo refraction along the y' direction as a function of f. It is interesting to note that in this case the permittivity along the y' direction is the inverse of the scalar effective permittivity for an array of perfect magnetic conductors [1] (that is, cylinders with Dirichlet boundary conditions). Equations (37) correspond to the square of the semiminor and semimajor axes of the index ellipse [49]:

$$\frac{x'^2}{\varepsilon_{x'}} + \frac{y'^2}{\varepsilon_{y'}} = 1. \tag{38}$$

From this, we expect elliptical solutions for the dispersion of light with eccentricity:
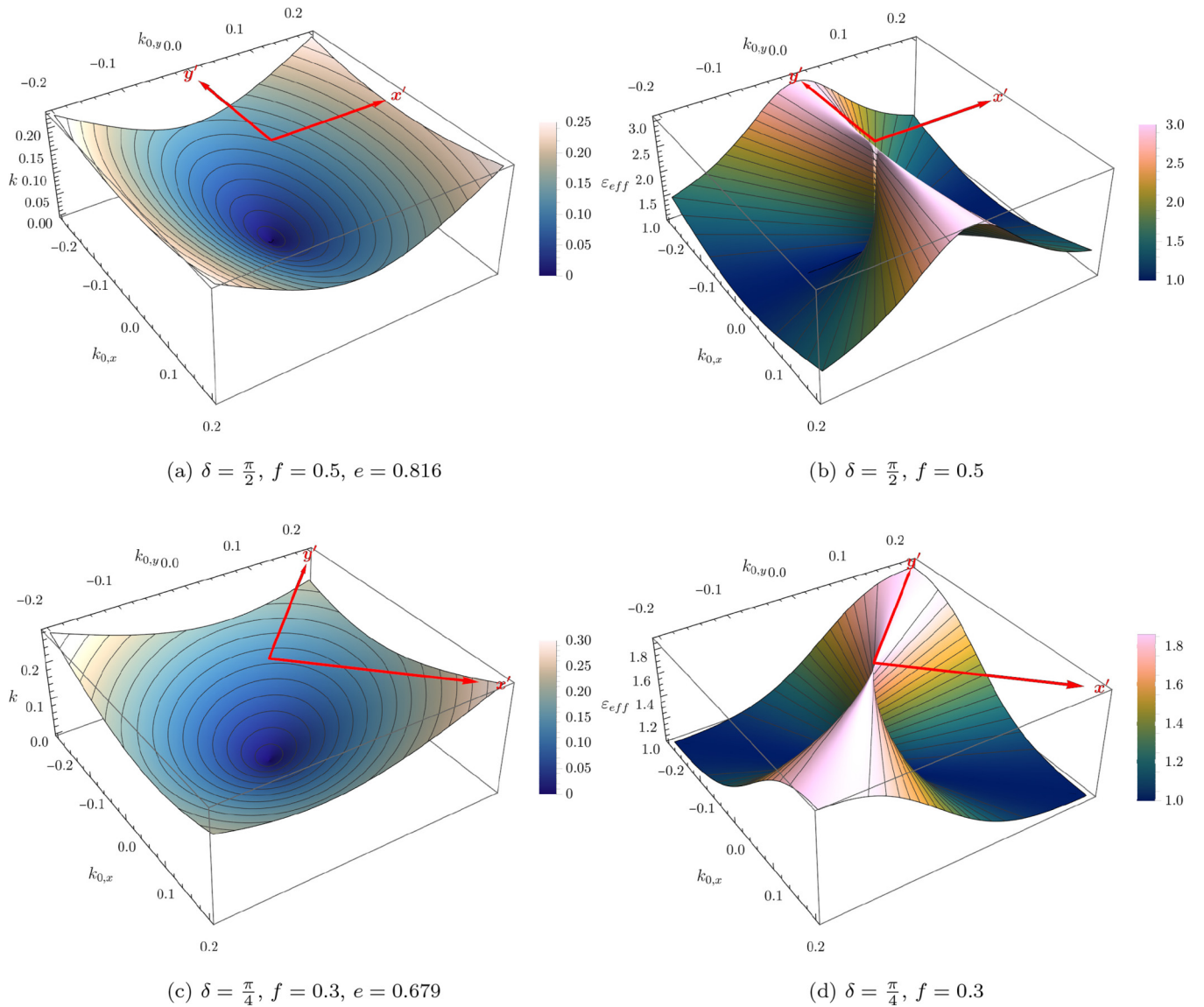
$$e = \sqrt{\frac{2f}{1+f}}, \tag{39}$$

(a) $\delta = \frac{\pi}{2}$, $f = 0.5$, $e = 0.816$

(b) $\delta = \frac{\pi}{2}$, $f = 0.5$

(c) $\delta = \frac{\pi}{4}$, $f = 0.3$, $e = 0.679$

(d) $\delta = \frac{\pi}{4}$, $f = 0.3$

FIG. 3. First dispersion surface $k = \alpha k_0$ and corresponding effective permittivity ε_{eff} for parameters (a), (b) $\delta = \pi/2$, $f = 0.5$ and (c), (d) $\delta = \pi/4$, $f = 0.3$ in the portion of the Brillouin zone $(k_{0,x}, k_{0,y}) \in [-0.2, 0.2]$. Principle axes are labeled in red.

which increases with larger area fraction f. Equation (39) tends to zero as $f \to 0$, meaning isotropy is recovered at small area fraction because the scattering is so weak.

The anisotropy of the crystal is visualized by the first dispersion surfaces in Figs. 3(a) and 3(c) and the corresponding effective permittivities in Fig. 3(b) and 3(d) for parameters (a),(b) $\delta = \pi/2$, $f = 0.5$ and (c),(d) $\delta = \pi/4$, $f = 0.3$. Examining first the dispersion surfaces (a),(c) we observe that the eccentricity of the elliptical surface contours falls from $e = 0.816$ when $f = 0.5$ to $e = 0.679$ when $f = 0.3$, a consequence of the scattering by the metacylinders being weaker at smaller area fraction. Complementary to

these are the permittivity surfaces (b),(d), which illustrate how the transport of light through the crystal is subject to its propagation direction, with the values along the x' and y' axes equaling those calculated by (37) i.e., transparent along x' and at a maximum along y'.

B. The case $n_r \neq 1$

In the case of $n_r \neq 1$ the leading order term in the expansion of $|\mathbf{T}|$ is of the form

$$T_{-12} = \frac{2^{14}\pi^2 e^{2i\delta}(2n_r^2 + 1)\{n_r^2(f^2 - 1) - f^2 - 1 - 2f\cos[2(\delta - \theta_0)] + (1 + f)[n_r^2 + 1 + f(n_r^2 - 1)]\alpha_0^2\}}{n_r^2 f^6 k_0^{12} d^{12} \alpha_0^{12}(\alpha_0^2 - 1)}. \tag{40}$$

Equating the left-hand side to zero and solving for α_0 gives

$$\alpha_0 = \sqrt{\frac{n_r^2 + 1 - f^2(n_r^2 - 1) + 2f\cos[2(\delta - \theta_0)]}{n_r^2(1 + f)^2 - f^2 + 1}}. \quad (41)$$

The corresponding Maxwell Garnett equation is

$$\varepsilon_{\text{eff}}^0 = \frac{n_r^2(1 + f)^2 - f^2 + 1}{n_r^2 + 1 - f^2(n_r^2 - 1) + 2f\cos[2(\delta - \theta_0)]}, \quad (42)$$

such that along the principal axes

$$\varepsilon_{x'} = \frac{n_r^2(1 + f)^2 - f^2 + 1}{n_r^2 + 1 - f^2(n_r^2 - 1) + 2f}, \quad (43a)$$

$$\varepsilon_{y'} = \frac{1 + f}{1 - f}. \quad (43b)$$

Equations (43) admit elliptical solutions of eccentricity:

$$e = \sqrt{\frac{4f}{(1 + f)(n_r^2(1 - f) + f + 1)}}, \quad (44)$$

which trivially reduces to (39) when $n_r = 1$, as do Eqs. (41)–(43) reduce to their $n_r = 1$ counterparts. Note that due to the presence of n_r^2 in the denominator of (44) the eccentricity of the elliptical dispersion surfaces will fall for n_r increasing and rise for n_r decreasing. In other words, a lattice of large material contrast will tend to either the isotropic of anisotropic scattering of light depending on the composition of the interior material relative to that of the exterior. In fact, if we replace n_r^2 by

$$n_r^2 = \frac{\tau + 1}{\tau - 1} \quad (45)$$

in (23), where $1/\tau$ represents the "dielectric contrast" across the interface between the interstitial dielectric and the exterior bulk [2], we arrive to

$$\alpha_0 = \sqrt{\frac{\tau - f^2 + f(\tau - 1)\cos[2(\delta - \theta)]}{(1 + f)(f + \tau)}}. \quad (46)$$

Then along x'

$$\varepsilon_{x'} = \frac{\tau + f}{\tau - f}, \quad (47)$$

and $\varepsilon_{y'} = (1 + f)/(1 - f)$ as before. Equation (47) is of the form of the Lorentz-Lorenz or Clausius-Mossotti equation for an array of dielectric cylinders [1,46] and obeys Keller's theorem [50]; by replacing τ with $-\tau$ we obtain $1/\varepsilon_{x'}$ along x'. Keller's theorem is not obeyed along any other direction due to the anisotropy induced by the plate-array, which is expressed through the $\cos[2(\delta - \theta)]$ term at leading order.

The effects of a nonunity material contrast on the anisotropic dispersion of light is visualized in Fig. 4 for $\delta = \pi/2$ and $f = 0.5$ for relative index (a),(b) $n_r = 3$ and (c),(d) $n_r = 1/3$. Examining the dispersion surfaces, Figs. 4(a) and 4(c), we note that the eccentricity has fallen in the case of $n_r = 3$ with respect to the result quoted in Fig. 3(a) under the same area fraction, and likewise increased with respect to the same result in the case of $n_r = 1/3$. The respective permittivity surfaces, Figs. 4(b) and 4(d), illustrate the same

effect, with the effective permittivity in Fig. 4(b) varying more smoothly between x' and y' than in Fig. 4(d).

This parameter space is explored in Fig. 5 in which the effective permittivity, as approximated by the Maxwell Garnett equation (42), is plotted over the range of relative angle $\delta - \theta_0 \in [0, \pi]$ for varying (a)–(c) f and (d)–(f) n_r. These types of phase portraits are useful for visualising the steepness in the effective permittivity between the principal axes at $\delta - \theta_0 = 0$ and $\delta - \theta_0 = \pi/2$, and in this way illustrate the strength of the anisotropic scattering of light by the crystal. Figures 5(a)–5(c) demonstrate how the eccentricity of the resulting elliptical dispersion surfaces falls as the relative refractive index is increased from $n_r = 1/3$ to $n_r = 3$, as the surface contours flatten and widen across the angular range. Likewise in Figs. 5(d)–5(f) an increase in the area fraction f gives rise to narrowing surface contours about $\delta - \theta_0 = \pi/2$.

C. Numerical validation

In order to validate the leading order approximations (35) and (41), we carry out a comparison between a numerical implementation of system (22) truncated at $M = 6$, and a finite element (FEM) implementation. These codes are available in the Supplemental Material [48]. Provided in Figs. 6(a) and 6(b) is the portion of the acoustic band along $N \rightarrow \Gamma \rightarrow X$ (see inset) for a plate-array cylinder aligned at angle $\delta = \pi/2$, such that the path within the Brillouin zone follows the principal crystalline axes. Panel (a) depicts the acoustic band as a function of f and panel (b) as a function of n_r. The FEM computations were carried out using COMSOL MULTIPHYSICS [51], for which a cylinder of 100 plates of thickness $w_p = a/100$ and interplate spacing $d_p = a/100$ was used.

Overall there is good agreement between the leading order approximations and the multipole and FEM computations, particularly as $k, k_0 \rightarrow 0$. In the case of $n_r = 1$ [Fig. 6(a)] the approximation (35) is exact along $N \rightarrow \Gamma$ for which $\theta_0 = \delta$ and $\alpha_{x'} = 1$. On $\Gamma \rightarrow X$, $\theta_0 = \delta + \pi/2$ and $\alpha_{y'} \approx \sqrt{(1 - f)/(1 + f)}$. In this direction the divergence away from linear increases as the area fraction approaches its maximum value of $f = 0.5$ (black line), for which the quasistatic approximation remains accurate until $k \approx 1$; even when the crystal is not dilute the quasistatic approximation remains a good estimation of the acoustic band's gradient as $k_0 \rightarrow 0$.

In the case of $n_r \neq 1$ [Fig. 6(b) for which $f = 0.3$] the acoustic band along $N \rightarrow \Gamma$ is perturbed away from the light line as the relative index is moved away from unity. The divergence between the linear and the multipole/FEM computations is also a function of the relative index, although in both cases shown the linear approximation remains accurate until $k \approx 2$. Along $\Gamma \rightarrow X$ the divergence between the quasistatic and multipole and FEM treatments can also be ascribed to the relative index, which plays a role exclusively in the higher order term α_2 along y'. In the case $n_r = 2$, although we approach the resonance at $k = 2.5416$, the acoustic band, as computed by the multipole method, converges to the FEM result at $M = 6$. There is some divergence between the multipole and FEM computations in the case of $n_r = 1/2$, although this is likely due to the finite inter-plate spacing and plate number used in the FEM computations.
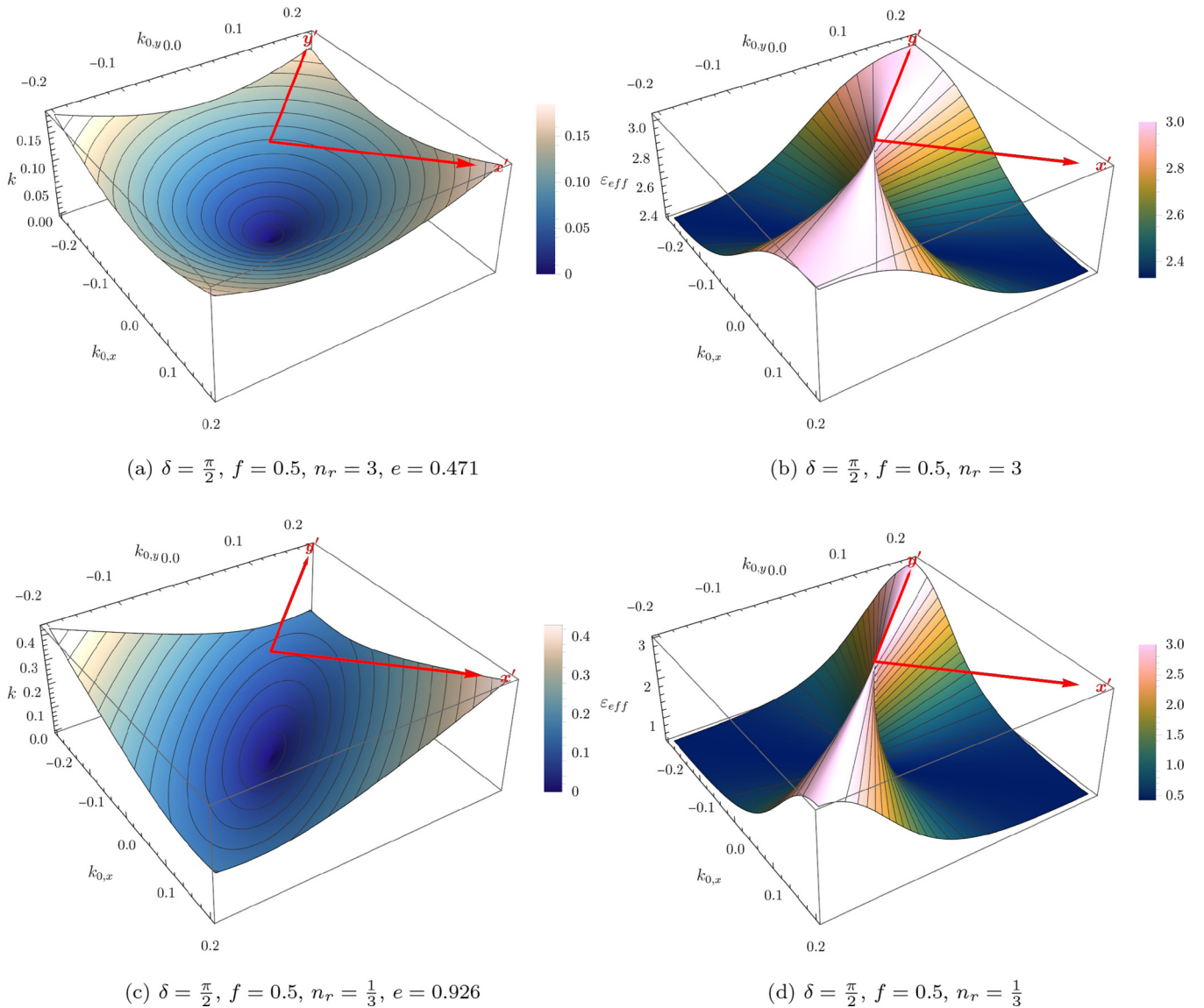
(a) $\delta = \frac{\pi}{2}$, $f = 0.5$, $n_r = 3$, $e = 0.471$

(b) $\delta = \frac{\pi}{2}$, $f = 0.5$, $n_r = 3$

(c) $\delta = \frac{\pi}{2}$, $f = 0.5$, $n_r = \frac{1}{3}$, $e = 0.926$

(d) $\delta = \frac{\pi}{2}$, $f = 0.5$, $n_r = \frac{1}{3}$

FIG. 4. First dispersion surface $k = \alpha k_0$ and corresponding effective permittivity ε_{eff} for parameters $\delta = \pi/2$, $f = 0.5$ and (a),(b) $n_r = 3$, (c),(d) $n_r = 1/3$ in the portion of the Brillouin zone $(k_{0,x}, k_{0,y}) \in [-0.2, 0.2]$. Principle axes are labeled in red.

VI. CONCLUDING REMARKS

In this paper we have presented a periodic medium of plate-array metacylinders which, in treating the plate-array as an effective medium, has been reduced to an elegant and computationally efficient semianalytical formalism. The periodic structure comprises a mechanically tunable metamaterial wherein the principal axes' orientation is dictated by the uniform plate-array angle. A dipole system approximates the acoustic band as $k, k_0 \to 0$, for which a pair of leading order Maxwell Garnett equations describe the medium's principal effective permittivities in terms of the area fraction f and relative index n_r.

Although there is good agreement between the quasistatic approximations and multipole and FEM treatments, the leading order approximations fail to capture the wave number dependence of α. The higher order term α_2 is necessary to resolve the quadratic behavior of the acoustic band at higher wave numbers, as depicted in Figs. 6(a) and 6(b). The

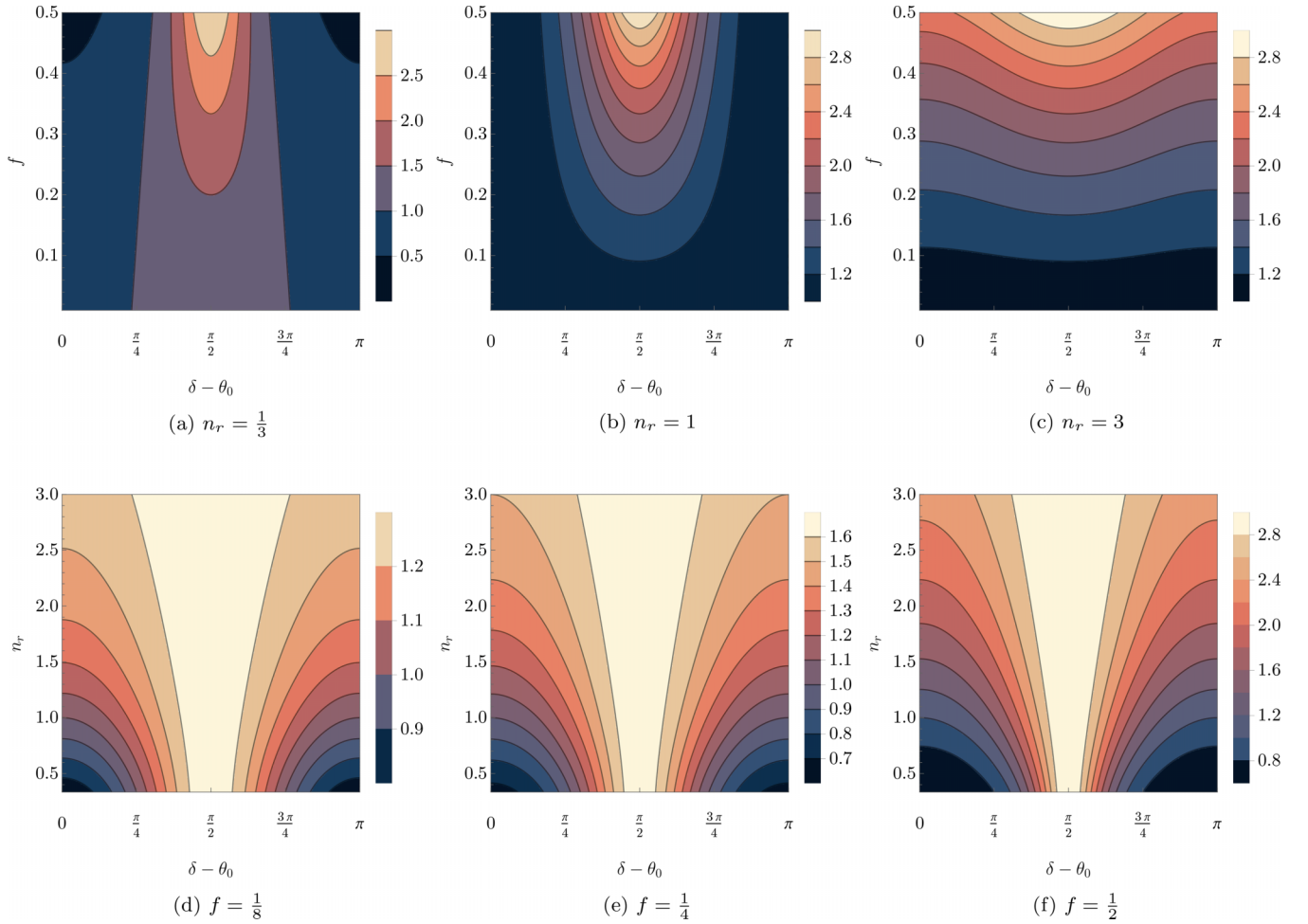determination of this higher order correction is left as an open problem.

FIG. 5. $\varepsilon_{\text{eff}}^0$ plotted as a function of (a)–(c) varying f and constant n_r (labeled) and (d)–(f) varying n_r and constant f (labeled). All solutions are symmetric by virtue of the $2\cos[2(\delta - \theta_0)]$ term in (42). Note the change in color scale from panel to panel.

APPENDIX A: PLATE-ARRAY HOMOGENIZATION

Under rotation to the primed cylinder coordinates (x', y') the Helmholtz equation in the interior domain (15) is

$$\left(\frac{\partial^2}{\partial x'^2} + \frac{\partial^2}{\partial y'^2} + n_r^2 k^2\right) H_z^{\text{int}}(x', y') = 0 \quad \text{(A1)}$$

and the boundary condition on the perfectly conducting plates is of the form

$$\frac{\partial}{\partial y'} H_z^{\text{int}}(x', \pm n d_p) = 0 \quad \text{(A2)}$$

for all $n \in \mathbb{Z}$, which represents the plates in both directions about the center of the plate array. We introduce the new coordinate y'' where $0 < y'' < 1$, such that any point in the interstitial medium can be written as $(x', y') \equiv (x', n d_p + d_p y'')$. In double-primed coordinates (A1) reads

$$\left(\frac{1}{n_r^2 k^2} \frac{\partial^2}{\partial x'^2} + \frac{1}{\zeta^2} \frac{\partial^2}{\partial y''^2} + 1\right) H_{n,z}^{\text{int}}(x', y'') = 0 \quad \text{(A3)}$$

with plate boundary condition

$$\frac{\partial}{\partial y''} H_{n,z}^{\text{int}} = 0 \quad \text{on } y'' = 0, \ 1, \quad \text{(A4)}$$

where the subscript denotes the interstitial space between the nth plate and its nearest neighbor. Note that the small parameter $\zeta = n_r k d_p$ remains small at finite n_r as long as $k d_p \ll 1$. By expanding the solution in powers of the small parameter squared,

$$H_{n,z}^{\text{int}}(x', y'') = H_n^0(x', y'') + \zeta^2 H_n^1(x', y'') + \mathcal{O}(\zeta^4), \quad \text{(A5)}$$

then at leading order (A3) is $\partial^2/\partial y''^2 (H_n^0) = 0$. As (A4) applies at all orders of the field expansion (A5) we surmise that $H_n^0 \equiv H_n^0(x')$ only. At next order (A3) reads

$$\left(\frac{\partial^2}{\partial x'^2} + n_r^2 k^2\right) H_n^0(x') + n_r^2 k^2 \frac{\partial^2 H_n^1}{\partial y''^2} = 0 \quad \text{(A6)}$$

whereby integration over y'' in $0 \leqslant y'' \leqslant 1$ and making use of the boundary condition (A4) yields

$$\left(\frac{\partial^2}{\partial x'^2} + n_r^2 k^2\right) H_n^0(x', y') = 0, \quad \text{(A7)}$$

which is just (15). Equation (A7) makes clear that the interior field is approximated by its leading order term in the power series expansion (A5), and that any dependence on the y' coordinate is not sensitive to changes over the scale $d_p y''$. See [29,30,38].
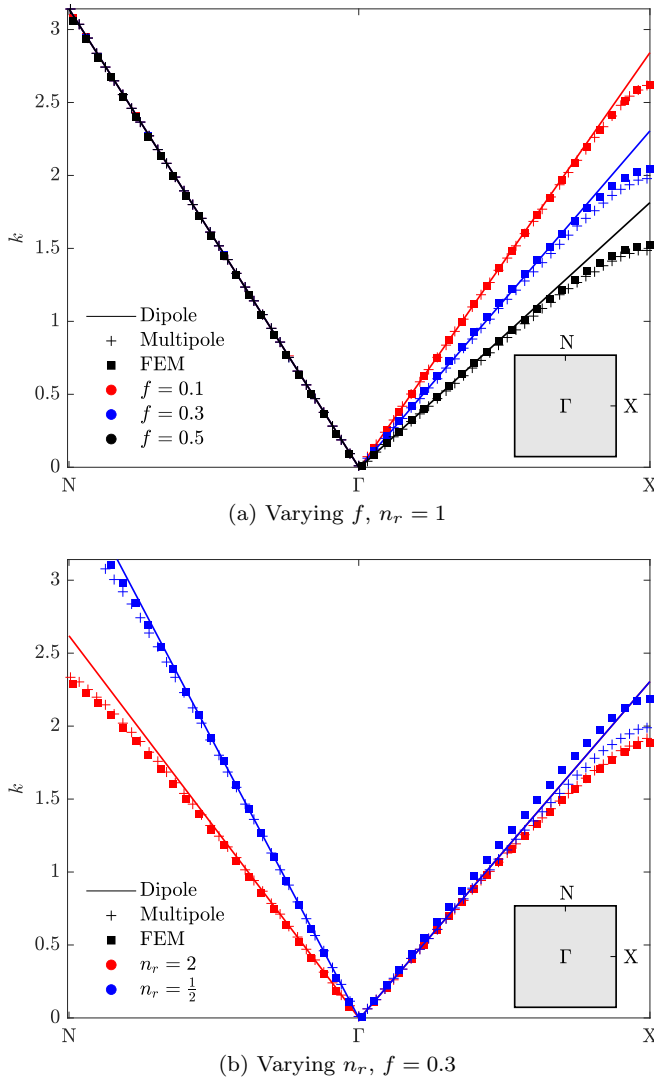
FIG. 6. Acoustic bands for a plate-array cylinder of angle $\delta = \pi/2$. Shown are the linear Dipole approximations (35) and (41) (solid lines), the multipole system (22) (crosses), and FEM computations (squares).

APPENDIX B: APPROXIMATE FORMULAS

1. Approximations of boundary coefficients

The boundary coefficients (24a) are approximated as the following series expansions in small k for $p \in [0, 1, 2]$:

$$M_0 = \frac{2\gamma}{\pi} + \frac{2}{\pi} \log\left(\frac{ka}{2}\right), \tag{B1a}$$

$$M_1 = -\frac{4}{\pi(ka)^2} + \frac{-3+4\gamma}{2\pi} + \frac{2}{\pi} \log\left(\frac{ka}{2}\right), \tag{B1b}$$

$$M_2 = -\frac{32}{\pi(ka)^4} - \frac{32}{3\pi(ka)^2} + \frac{-83+72\gamma}{36\pi} + \frac{2}{\pi} \log\left(\frac{ka}{2}\right), \tag{B1c}$$

and

$$M_0' = -\frac{4}{\pi(ka)^2} + \frac{-3+4\gamma}{2\pi} + \frac{2}{\pi} \log\left(\frac{ka}{2}\right), \tag{B2a}$$

$$M_1' = \frac{4}{\pi(ka)^2} + \frac{5+4\gamma}{2\pi} + \frac{2}{\pi} \log\left(\frac{ka}{2}\right), \tag{B2b}$$

$$M_2' = \frac{32}{\pi(ka)^4} + \frac{16}{3\pi(ka)^2} + \frac{5+72\gamma}{36\pi} + \frac{2}{\pi} \log\left(\frac{ka}{2}\right). \tag{B2c}$$

All approximations (B1), (B2) have been truncated so as to exclude all terms of $\mathcal{O}(ka)^2$.

2. Approximations of interior coefficients

The interior coefficients (24b) and (24c) are approximated as the following series expansions in small k for $p \in [-2, \ldots, 1]$, $n \in [0, 1]$:

$$\{C_{-2,0}, D_{-2,0}\} = e^{2i\delta} n_r^2 \left(1 - \frac{1}{12}(ka)^2(n_r^2 - 1)\right), \tag{B3a}$$

$$\{C_{-2,1}, D_{-2,1}\} = e^{2i\delta} n_r \left(\pm \frac{2}{ka} \mp \frac{1}{6}(ka)(n_r^2 - 1)\right), \tag{B3b}$$

$$\{C_{-1,0}, D_{-1,0}\} = ie^{i\delta} n_r \left(\pm 1 \mp \frac{1}{8}(ka)^2(n_r^2 - 1)\right), \tag{B3c}$$

$$\{C_{-1,1}, D_{-1,1}\} = ie^{i\delta} \left(\frac{1}{ka} - \frac{1}{8}(ka)(n_r^2 - 1)\right), \tag{B3d}$$

$$\{C_{0,0}, D_{0,0}\} = -1 + \frac{1}{4}(ka)^2(n_r^2 - 1), \tag{B3e}$$

$$\{C_{0,1}, D_{0,1}\} = 0, \tag{B3f}$$

$$\{C_{1,0}, D_{1,0}\} = ie^{-i\delta} n_r \left(\mp 1 \pm \frac{1}{8}(ka)^2(n_r^2 - 1)\right), \tag{B3g}$$

$$\{C_{1,1}, D_{1,1}\} = ie^{-i\delta} \left(\frac{1}{ka} - \frac{1}{8}(ka)(n_r^2 - 1)\right), \tag{B3h}$$

and

$$\{C_{-2,0}', D_{-2,0}'\} = e^{2i\delta} n_r \left(1 - \frac{1}{6}(ka)^2(n_r^2 - 1)\right), \tag{B4a}$$

$$\{C_{-2,1}', D_{-2,1}'\} = e^{2i\delta} n_r \left(\pm \frac{1}{ka} \mp \frac{1}{12}(ka)(3n_r^2 - 2)\right), \tag{B4b}$$

$$\{C_{-1,0}', D_{-1,0}'\} = ie^{i\delta} \left(\pm 1 \mp \frac{3}{8}(ka)^2(n_r^2 - 1)\right), \tag{B4c}$$

$$\{C_{-1,1}', D_{-1,1}'\} = -ie^{i\delta} \frac{1}{4}(ka) n_r, \tag{B4d}$$

$$\{C_{0,0}', D_{0,0}'\} = n_r \left(-1 + \frac{1}{8}(ka)^2(n_r^2 - 1)\right), \tag{B4e}$$

$$\{C_{0,1}', D_{0,1}'\} = 0, \tag{B4f}$$

$$\{C_{1,0}', D_{1,0}'\} = ie^{-i\delta} \left(\mp 1 \pm \frac{3}{8}(ka)^2(n_r^2 - 1)\right), \tag{B4g}$$

$$\{C_{1,1}', D_{1,1}'\} = -ie^{-i\delta} \frac{3}{8}(ka) n_r. \tag{B4h}$$

All approximations (B3), (B4) have been truncated so as to exclude all terms of $\mathcal{O}(ka)^3$.

3. Approximations of lattice sums

The following method for approximating the lattice sums (13) follows that set out by Poulton [40]. By separating the $h = 0$ and $h \neq 0$ terms and making use of Graf's addition theorem [34] on the latter summation, we arrive to the expression

$$S_l^Y = -\frac{Y_0(k\xi)}{J_0(k\xi)}\delta_{l,0} - i^l\frac{4}{d^2}\frac{e^{il\theta_0}}{k_0^2 - k^2}\frac{J_l(k_0\xi)}{J_l(k\xi)} - \frac{i^l}{J_l(k\xi)}\frac{4}{d^2}\sum_{h\neq 0}\sum_{m\in\mathbb{Z}}\frac{(-1)^m J_{l+m}(K_h\xi)J_m(k_0\xi)e^{i(l+m)\psi_h - im\theta_0}}{Q_h^2 - k^2},\tag{B5}$$

where $\mathbf{K}_h = (K_h, \psi_h)$. The denominators $(Q_h^2 - k^2)^{-1}$ are approximated by the expansion in small k as

$$\left(Q_h^2 - k^2\right)^{-1} = K_h^{-2}\left(1 - 2\frac{k_0}{K_h}\cos(\psi_h - \theta_0) + 2\frac{k_0^2}{K_h^2}\cos(2(\psi_h - \theta_0)) + \frac{k_0^2 + k^2}{K_h^2}\right).\tag{B6}$$

By combining (B5) and (B6) we obtain the approximation formulas for the lattice sums of all requisite orders 0–3. Orders 0–2 are available in Chap. 4 of [40]. Order 3 is approximated as

$$S_3^Y \approx \frac{4ie^{3i\theta_0}}{d^2}\left\{\frac{1}{k_0^2 - k^2}\frac{J_3(k_0\xi)}{J_3(k\xi)} - k_0 d^3 S_{1,0,3}\frac{J_2(k_0\xi)}{J_3(k\xi)} + k_0^2 d^4 S_{2,0,4}\frac{J_1(k_0\xi)}{J_3(k\xi)}\right\}$$
$$+ \frac{4ie^{-i\theta_0}}{d^2}\left\{\left(k_0^2 d^4 S_{2,4,4} - d^2 S_{4,4,2} - (k_0^2 + k^2)d^4 S_{4,4,4}\right)\frac{J_1(k_0\xi)}{J_3(k\xi)} - k_0 d^3 S_{3,4,3}\frac{J_0(k_0\xi)}{J_3(k\xi)} - k_0 d^3 S_{5,4,3}\frac{J_2(k_0\xi)}{J_3(k\xi)}\right\},\tag{B7}$$

where

$$S_{l,m,n}(\xi) = \sum_{h\neq 0}\frac{J_l(K_h\xi)e^{im\psi_h}}{(K_h d)^n}.\tag{B8}$$

Expressions for sums of the form (B8) are found using the lattice sum recurrence relations found in Chap. 3 of [40]. The remaining sums not found in [40] are of the form

$$S_{4,4,4} = \frac{\tilde{\sigma}_2^{(4)}}{12\pi}\left(\frac{\xi}{2d}\right)^4 - \frac{\sigma_4^{(4)}}{5\pi}\left(\frac{\xi}{2d}\right)^6,\tag{B9a}$$

$$S_{5,4,3} = \frac{\sigma_4^{(4)}}{5\pi}\left(\frac{\xi}{2d}\right)^5,\tag{B9b}$$

where the quantities $\tilde{\sigma}_2^{(4)} = 4.078\,451\,161\,161\,4 - \pi/2$ and $\sigma_4^{(4)} = 3.151\,212\,002\,153\,9$ are numerical evaluations of static lattice sums [52]. Combining (B7), (B9) and the remaining sums found in [40], and making use of series expansions for the ratios of Bessel functions embedded in (B7), we obtain

$$S_3^Y = \frac{4i}{d^2}\frac{k_0^3}{k^3}\left\{e^{3i\theta_0}\left(\frac{1}{k_0^2 - k^2} + \frac{3d^2}{8\pi}\right) + e^{-i\theta_0}\left(\frac{3d^2\tilde{\sigma}_2^{(4)}}{4\pi^2} - \frac{2\tilde{\sigma}_2^{(4)}}{\pi k_0^2}\right)\right\},\tag{B10}$$

which is correct to $\mathcal{O}(k^0)$. The approximation (B10) has undergone validation by numerical comparison with the accelerated summation of (13).

---

[1] A. B. Movchan, N. V. Movchan, and C. G. Poulton, *Asymptotic Models of Fields in Dilute and Densely Packed Composites* (World Scientific, Singapore, 2002), Chap. 3.

[2] R. C. McPhedran, C. G. Poulton, N. A. Nicorovici, and A. B. Movchan, Low frequency corrections to the static effective dielectric constant of a two-dimensional composite material, Proc. R. Soc. London A **452**, 2231 (1996).

[3] S. O'Brien and J. Pendry, Magnetic activity at infrared frequencies in structured metallic photonic crystals, J. Phys.: Condens. Matter **14**, 6383 (2002).

[4] D. Schurig, J. J. Mock, and D. R. Smith, Electric-field-coupled resonators for negative permittivity metamaterials, Appl. Phys. Lett. **88**, 041109 (2006).

[5] S. Tretyakov, Meta-materials with wideband negative permittivity and permeability, Microw. Opt. Technol. **31**, 163 (2001).

[6] D. R. Smith, W. J. Padilla, D. C. Vier, S. C. Nemat-Nasser, and S. Schultz, Composite medium with simultaneously negative permeability and permittivity, Phys. Rev. Lett. **84**, 4184 (2000).

[7] D. R. Smith and N. Kroll, Negative refractive index in left-handed materials, Phys. Rev. Lett. **85**, 2933 (2000).

[8] J. B. Pendry, Negative refraction makes a perfect lens, Phys. Rev. Lett. **85**, 3966 (2000).

[9] J. B. Pendry, D. Schurig, and D. R. Smith, Controlling electromagnetic fields, Science **312**, 1780 (2006).

[10] G. W. Milton and N.-A. P. Nicorovici, On the cloaking effects associated with anomalous localized resonance, Proc. R. Soc. A. **462**, 3027 (2006).

[11] C. Luo, S. G. Johnson, J. D. Joannopoulos, and J. B. Pendry, All-angle negative refraction without negative effective index, Phys. Rev. B **65**, 201104(R) (2002).

[12] F. Crameri, Scientific colour maps, Zenodo (2018), doi: 10.5281/zenodo.8035877.

[13] K. Fan, R. D. Averitt, and W. J. Padilla, Active and tunable nanophotonic metamaterials, Nanophotonics **11**, 3769 (2022).

[14] M. J. Smith and I. D. Abrahams, Tailored acoustic metamaterials. Part I. Thin-and thick-walled Helmholtz resonator arrays, Proc. R. Soc. A. **478**, 20220124 (2022).

[15] M. J. Smith and I. D. Abrahams, Tailored acoustic metamaterials. Part II. Extremely thick-walled Helmholtz resonator arrays, Proc. R. Soc. A. **478**, 20220125 (2022).

[16] C.-W. Qiu, T. Zhang, G. Hu, and Y. Kivshar, Quo vadis, metasurfaces? Nano Lett. **21**, 5461 (2021).

[17] R. Kumar and K. Kajikawa, Superscattering from cylindrical hyperbolic metamaterials in the visible region, Opt. Express **28**, 1507 (2020).

[18] C. P. Mavidis, A. C. Tasolamprou, E. N. Economou, C. M. Soukoulis, and M. Kafesaki, Single scattering and effective medium description of multilayer cylinder metamaterials: Application to graphene-and to metasurface-coated cylinders, Phys. Rev. B **107**, 134120 (2023).

[19] J. P. Turpin, J. A. Bossard, K. L. Morgan, D. H. Werner, and P. L. Werner, Reconfigurable and tunable metamaterials: A review of the theory and applications, Int. J. Antennas Propag. **2014**, 18 (2014).

[20] A. D. Boardman, V. V. Grimalsky, Y. S. Kivshar, S. V. Koshevaya, M. Lapine, N. M. Litchinitser, V. N. Malnev, M. Noginov, Y. G. Rapoport, and V. M. Shalaev, Active and tunable metamaterials, Laser Photonics Rev. **5**, 287 (2011).

[21] I. M. Pryce, K. Aydin, Y. A. Kelaita, R. M. Briggs, and H. A. Atwater, Highly strained compliant optical metamaterials with large frequency tunability, Nano Lett. **10**, 4222 (2010).

[22] S. Walia, C. M. Shah, P. Gutruf, H. Nili, D. R. Chowdhury, W. Withayachumnankul, M. Bhaskaran, and S. Sriram, Flexible metasurfaces and metamaterials: A review of materials and fabrication processes at micro-and nano-scales, Appl. Phys. Rev. **2**, 011303 (2015).

[23] H.-S. Ee and R. Agarwal, Tunable metasurface and flat optical zoom lens on a stretchable substrate, Nano Lett. **16**, 2818 (2016).

[24] W. Park and J.-B. Lee, Mechanically tunable photonic crystal structure, Appl. Phys. Lett. **85**, 4845 (2004).

[25] J. T. Overvelde, T. A. De Jong, Y. Shevchenko, S. A. Becerra, G. M. Whitesides, J. C. Weaver, C. Hoberman, and K. Bertoldi, A three-dimensional actuated origami-inspired transformable metamaterial with multiple degrees of freedom, Nat. Commun. **7**, 10929 (2016).

[26] H. Tao, A. C. Strikwerda, K. Fan, W. J. Padilla, X. Zhang, and R. D. Averitt, Reconfigurable terahertz metamaterials, Phys. Rev. Lett. **103**, 147401 (2009).

[27] M. Baraclough, I. R. Hooper, and W. L. Barnes, Investigation of the coupling between tunable split-ring resonators, Phys. Rev. B **98**, 085146 (2018).

[28] G. J. Chaplain, A. S. Gliozzi, B. Davies, D. Urban, E. Descrovi, F. Bosia, and R. V. Craster, Tunable topological edge modes in Su-Schrieffer-Heeger arrays, Appl. Phys. Lett. **122**, 221703 (2023).

[29] H. J. Putley, S. Guenneau, R. Porter, and R. V. Craster, A tunable electromagnetic metagrating, Proc. R. Soc. A. **478**, 20220454 (2022).

[30] S. Zheng, R. Porter, and D. Greaves, Wave scattering by an array of metamaterial cylinders, J. Fluid Mech. **903**, A50 (2020).

[31] Ö. Kavaklioglu, On Schlömilch series representation for the transverse electric multiple scattering by an infinite grating of insulating dielectric circular cylinders at oblique incidence, J. Phys. A: Math. Gen. **35**, 2229 (2002).

[32] A. Sommerfeld, *Partial Differential Equations in Physics* (Academic, New York, 1949).

[33] W. Wijngaard, Guided normal modes of two parallel circular dielectric rods, J. Opt. Soc. Am. **63**, 944 (1973).

[34] M. Abramowitz and I. A. Stegun, *Handbook of Mathematical Functions*, 10th ed. (Dover, New York, 1964), p. 363.

[35] S. K. Chin, N. A. Nicorovici, and R. C. McPhedran, Green's function and lattice sums for electromagnetic scattering by a square array of cylinders, Phys. Rev. E **49**, 4590 (1994).

[36] R. C. McPhedran, N. A. Nicorovici, L. C. Botten, and B. Ke-Da, Green's function, lattice sums and Rayleigh's identity for a dynamic scattering problem, *Wave propagation in complex media*, in *Wave Propagation in Complex Media* (Springer, New York, 1998), p. 155.

[37] N. A. Nicorovici, R. C. McPhedran, and R. Petit, Efficient calculation of the Green's function for electromagnetic scattering by gratings, Phys. Rev. E **49**, 4563 (1994).

[38] R. Porter, Plate arrays as a perfectly-transmitting negative-refraction metamaterial, Wave Motion **100**, 102673 (2021).

[39] D. L. Colton and R. Kress, *Inverse Acoustic and Electromagnetic Scattering Theory*, Applied Mathematical Sciences (Springer, New York, 1998), Vol. 93.

[40] C. G. Poulton, Asymptotics and wave propagation in cylindrical geometries, Ph.D. thesis, University of Sydney, 1999.

[41] S. Guenneau, C. G. Poulton, and A. B. Movchan, Oblique propagation of electromagnetic and elastic waves for an array of cylindrical fibres, Proc. R. Soc. London A **459**, 2215 (2003).

[42] M. Abramowitz, I. A. Stegun, and R. H. Romer, *Handbook of Mathematical Functions with Formulas, Graphs, and Mathematical Tables* (American Association of Physics Teachers, 1988), Chap 9.

[43] N. A. Nicorovici, R. C. McPhedran, and L. C. Botten, Photonic band gaps for arrays of perfectly conducting cylinders, Phys. Rev. E **52**, 1135 (1995).

[44] N. A. Nicorovici, R. C. McPhedran, and L. C. Botten, Photonic band gaps: Noncommuting limits and the "acoustic band", Phys. Rev. Lett. **75**, 1507 (1995).

[45] R. C. McPhedran, N. A. Nicorovici, and L. C. Botten, The tem mode and homogenization of doubly periodic structures, J. Electromagn. Waves. Appl. **11**, 981 (1997).

[46] R. C. McPhedran, C. G. Poulton, N. A. Nicorovici, and A. B. Movchan, Dynamic corrections to the Lorentz-Lorenz formula, Physica A **241**, 179 (1997).

[47] *Mathematica, Version 13.3*, Wolfram Research, Inc., Champaign, Illinois, 2023, https://www.wolfram.com/mathematica.

[48] See Supplemental Material at http://link.aps.org/supplemental/10.1103/PhysRevB.108.214105 for the *Mathematica* script used to solve the dipole matrix determinant with symbolic algebra. The Supplemental Material also contains MATLAB scripts necessary for the numerical computation of the multipole method, and our FEM data computed with COMSOL MULTIPHYSICS®.

[49] M. Born and E. Wolf, *Principles of Optics: Electromagnetic Theory of Propagation, Interference and Diffraction of Light* (Elsevier, Amsterdam, 2013), Chap. 14.

[50] J. B. Keller, A theorem on the conductivity of a composite medium, J. Math. Phys. **5**, 548 (1964).

[51] *COMSOL Multiphysics®*, COMSOL AB, Stockholm, Sweden, 2023, https://www.comsol.com.

[52] A. B. Movchan, N. A. Nicorovici, and R. C. McPhedran, Green's tensors and lattice sums for electrostatics and elastodynamics, Proc. R. Soc. London A **453**, 643 (1997).